

A method to integrate and classify normal distributions

Abhranil Das ^{*1,2} and Wilson S Geisler^{2,3}

¹Department of Physics, The University of Texas at Austin

²Center for Perceptual Systems, The University of Texas at Austin

³Department of Psychology, The University of Texas at Austin

October 21, 2021

Abstract

Univariate and multivariate normal probability distributions are widely used when modeling decisions under uncertainty. Computing the performance of such models requires integrating these distributions over specific domains, which can vary widely across models. Besides some special cases where these integrals are easy to calculate, there exists no general analytical expression, standard numerical method or software for these integrals. Here we present mathematical results and software that provide (i) the probability in any domain of a normal in any dimensions with any parameters, (ii) the probability density, distribution, and percentage points of any function of a normal vector, (iii) quantities, such as the error matrix and discriminability, which summarize classification performance amongst any number of normal distributions, (iv) dimension reduction and visualizations for all such problems, and (v) tests for how reliably these methods can be used on given data. We illustrate these tools with models for detecting occluding targets in natural scenes and for detecting camouflage.

To compute the performance predicted by such theories it is necessary to integrate the normal distributions over specific domains. For example, a particularly common task in vision science is classification into two categories (such as detection and discrimination tasks), which is done using Gaussian discriminant analysis. The predicted maximum accuracy in such tasks is determined by integrating normals over domains defined by a quadratic decision boundary [1, 2]. Predicted accuracy of sub-optimal models is determined by integrating over other domains.

Except for some special cases where these integrals are easier to calculate [3, 4] (e.g. where two normals have equal covariance and the optimal classification boundary is flat), there exists no general analytical expression, numerical method or standard software tool to quickly and accurately integrate arbitrary normals over arbitrary domains, or to compute classification errors and the discriminability index d' . Evaluating these quantities thus frequently requires the limiting assumption of equal variance. This impedes the quick testing, comparison, and optimization of models. Here we describe a mathematical method and accompanying software implementation which provides functions to (i) integrate normals with arbitrary means and covariances in any number of dimensions over arbitrary domains, (ii) compute the pdf, cdf and inverse cdf of any function of a multinormal variable (normal vector), and (iii) compute the performance of classifying amongst any number of normals. This is available as an open-source Matlab toolbox ‘Integrate and classify normal distributions’, and at github.com/abhranildas/IntClassNorm.

We first review and assimilate previous mathematical results into a method to integrate arbitrary normals over quadratic domains. Then we present our method to integrate them over any domain, and consequently to compute the distribution of any real-valued function of a normal vector. We describe how these results can be used to compute error rates (and other relevant quantities) for Bayes-optimal and custom classifiers, given arbitrary priors and outcome cost matrix. We then present some methods to reduce problems to fewer dimensions, for analysis or visualization. Next, we provide a way to test whether directly measured samples from the actual distributions in a classification problem are close enough to normal to trust the computations from the toolbox. After

1 Introduction

The univariate or multivariate normal (henceforth called simply ‘normal’) is arguably the most important and widely-used probability distribution. It is frequently used because various central-limit theorems guarantee that normal distributions are frequently observed in nature, and because it is the simplest and most tractable distribution that allows arbitrary correlations between the variables.

Normal distributions form the foundation of many models/theories in the natural and social sciences. For example, they are the foundation of Bayesian statistical decision/classification theories, which are widely used in vision science, neuroscience, psychology and economics. These theories specify optimal performance under uncertainty, and are often used to provide a benchmark against which to evaluate the performance (behavior) of humans, other animals, neural circuits and algorithms. These theories also serve as a starting point in developing other models/theories that describe sub-optimal performance of agents.

*abhranil.das@utexas.edu

describing the methods and software toolbox with examples, we demonstrate their accuracy and speed across a variety of problems, and then illustrate them with two applications from our laboratory: modeling detection of occluding targets in natural scenes, and detecting camouflage.

2 Integrating the normal

2.1 In quadratic domains: the generalized chi-square method

Integrating the normal in quadratic domains is important for optimally classifying them. The problem is the following: given a column vector $\mathbf{x} \sim N(\boldsymbol{\mu}, \boldsymbol{\Sigma})$, find the probability that

$$q(\mathbf{x}) = \mathbf{x}'\mathbf{Q}_2\mathbf{x} + \mathbf{q}'_1\mathbf{x} + q_0 > 0. \quad (1)$$

This can be conceptualized as either integrating the normal probability over the domain $q(\mathbf{x}) > 0$ (the ‘normal probability picture’), or integrating the probability of the scalar-valued quadratic function $q(\mathbf{x})$ of a normal vector, beyond 0 (the ‘function probability picture’).

First, we linearly transform the space: $\mathbf{z} = \boldsymbol{\Sigma}^{-\frac{1}{2}}(\mathbf{x} - \boldsymbol{\mu})$. This standardizes the normal: $\mathbf{z} \sim N(\mathbf{0}, \mathbf{1})$, i.e. decorrelates the cues or whitens the signal, and transforms the integration domain to a different quadratic:

$$\begin{aligned} \tilde{q}(\mathbf{z}) &= \mathbf{z}'\tilde{\mathbf{Q}}_2\mathbf{z} + \tilde{\mathbf{q}}'_1\mathbf{z} + \tilde{q}_0 > 0, \text{ with} \\ \tilde{\mathbf{Q}}_2 &= \boldsymbol{\Sigma}^{\frac{1}{2}}\mathbf{Q}_2\boldsymbol{\Sigma}^{\frac{1}{2}}, \\ \tilde{\mathbf{q}}_1 &= \boldsymbol{\Sigma}^{\frac{1}{2}}(2\mathbf{Q}_2\boldsymbol{\mu} + \mathbf{q}_1), \\ \tilde{q}_0 &= q(\boldsymbol{\mu}). \end{aligned} \quad (2)$$

Now the problem is to find the probability of the standard normal \mathbf{z} in this domain. If there is no quadratic term $\tilde{\mathbf{Q}}_2$, $\tilde{q}(\mathbf{z})$ is normally distributed, the integration domain boundary is a flat, and the probability is $\Phi(\frac{\tilde{q}_0}{\|\tilde{\mathbf{q}}_1\|})$, where Φ is the standard normal cdf [3]. Otherwise, say $\tilde{\mathbf{Q}}_2 = \mathbf{R}\boldsymbol{\Lambda}\mathbf{R}'$ is its eigendecomposition, where \mathbf{R} is orthogonal, i.e. a roto-reflection. So $\mathbf{y} = \mathbf{R}'\mathbf{z}$ is also standard normal, and in this space the quadratic is:

$$\begin{aligned} \hat{q}(\mathbf{y}) &= \mathbf{y}'\boldsymbol{\lambda}\mathbf{y} + \mathbf{b}'\mathbf{y} + \tilde{q}_0 \quad (\mathbf{b} = \mathbf{R}'\tilde{\mathbf{q}}_1) \\ &= \sum_j (\lambda_j y_j^2 + b_j y_j) + \sum_{j'} b_{j'} y_{j'} + \tilde{q}_0 \\ &\quad (j \text{ and } j' \text{ index the nonzero and zero eigenvalues}) \\ &= \sum_j \lambda_j \left(y_j + \frac{b_j}{2\lambda_j} \right)^2 + \sum_{j'} b_{j'} y_{j'} + \tilde{q}_0 - \sum_j \left(\frac{b_j}{2\lambda_j} \right)^2 \\ &= \sum_i \lambda_i \chi_{m_i, \delta_i^2}^2 + \sigma z + c = \tilde{\chi}_{\boldsymbol{\lambda}, \mathbf{m}, \boldsymbol{\delta}, \sigma, c}^2 \end{aligned}$$

where $\tilde{\chi}^2$ is a generalized chi-square variable (a weighted sum of non-central chi-square variables χ'^2 with degrees of freedom m_i and non-centralities δ_i^2), a standard normal variable z , and a constant. The weights λ_i are the *unique* nonzero eigenvalues, m_i are the number of times they occur, and

$$\delta_i^2 = \frac{1}{4\lambda_i^2} \sum_{j:\lambda_j=\lambda_i} b_j^2, \quad \sigma^2 = \sum_{j'} b_{j'}^2, \quad c = \sum_i \lambda_i \delta_i^2 - \tilde{q}_0.$$

The required probability, $p(\tilde{\chi}^2 > 0)$, is now a 1d integral, computable using, say, Ruben’s [5] or Davies’ [6] methods.

We note that to the best of our knowledge, this complete general theory has not been described in the previous literature. Compared to previous software that implements specific forms of this theory for particular quadratics such as ellipsoids [4], this method correctly handles all quadratics (ellipsoids, hyperboloids, paraboloids and degenerate conics) in all dimensions.

2.2 In any domain: the ray-scan method

Since the normal distribution tails off infinitely outwards, it is inefficient to numerically integrate it over a finite uniform Cartesian grid, which would be large and collect ever-reducing masses outwards, yet omit some mass where it is truncated. Also, if the normal is elongated by unequal variances and strong covariances, or the integration domain is complex and non-contiguous, naïve integration grids will waste resources in regions or directions with low density. One then needs to visually inspect and arduously hand-tailor the integration grid to fit the problem shape.

Our method, presented below, standardizes the normal to symmetrize it, then divides the integration into polar coordinates that match this symmetry. The radial integral is calculated analytically, so it collects the entire mass to infinity without omission, machine imprecision, or using computation resources. The remaining integral is over an angular grid that is finite, so it can be done efficiently. The method is thus fast and accurate to arbitrary tolerance for all problem shapes without needing any manual adjustment.

2.2.1 Standard polar form

The problem is to find the probability that some general $f(\mathbf{x}) > 0$. As before, we first standardize the space to obtain $\tilde{f}(\mathbf{z}) = f(\boldsymbol{\Sigma}^{\frac{1}{2}}\mathbf{z} + \boldsymbol{\mu})$. Then we switch to polar axis-angle coordinates z and $\hat{\mathbf{n}}$: any point $\mathbf{z} = z\hat{\mathbf{n}}$, where the unit vector $\hat{\mathbf{n}}$ denotes the angle of that point, and z is its coordinate along the axis in this direction. Then the integral can be written as:

$$\int_{\tilde{\Omega}} (2\pi)^{-\frac{d}{2}} e^{-\frac{z^2}{2}} dz = \int_{\hat{\mathbf{n}}} d\hat{\mathbf{n}} \underbrace{\int_{\tilde{\Omega}_{\hat{\mathbf{n}}}} (2\pi)^{-\frac{d}{2}} e^{-\frac{z^2}{2}} dz}_{\text{axial integral}}$$

where $\tilde{\Omega}$ is the domain where $\tilde{f}(\mathbf{z}) > 0$, and $\tilde{\Omega}_{\hat{\mathbf{n}}}$ is its slice along the axis $\hat{\mathbf{n}}$, i.e. where $\tilde{f}_{\hat{\mathbf{n}}}(z) = \tilde{f}(z\hat{\mathbf{n}}) > 0$. This may be called the ‘standard polar form’ of the integral. $d\hat{\mathbf{n}}$ is the differential angle element ($d\theta$ in 2d, $\sin\theta d\theta d\phi$ in 3d etc).

2.2.2 Integration domain on a ray

First let us consider the axial integration at direction $\hat{\mathbf{n}}$. Imagine that we ‘scan’ the integration domain with a ‘ray’ at this direction (arrow in fig. 1a), to determine the part of the ray that is in the integration domain, defined by $\tilde{f}_{\hat{\mathbf{n}}}(z) = \tilde{f}(z\hat{\mathbf{n}}) > 0$. For example, if the integration domain

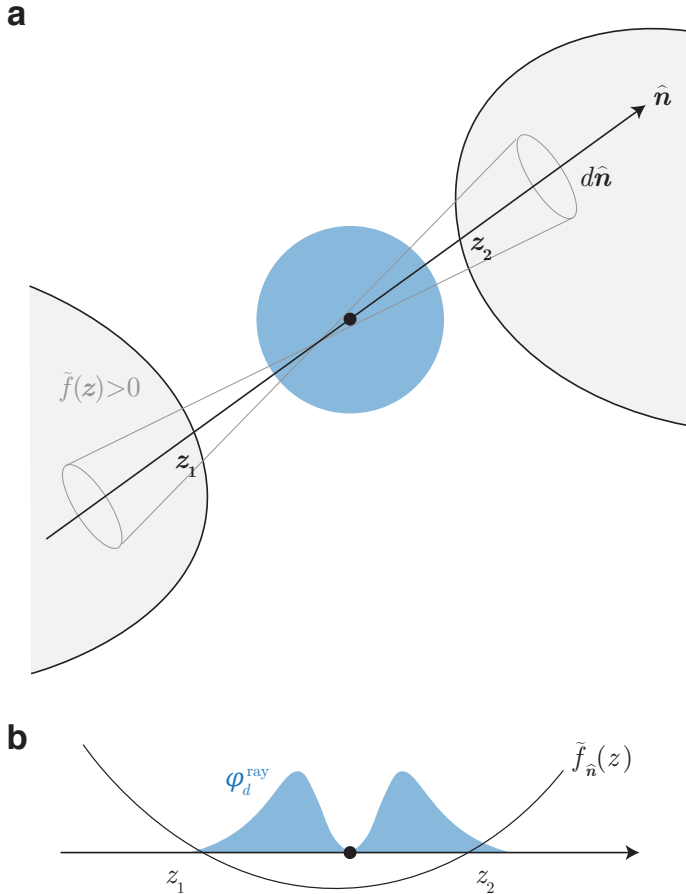


Figure 1: Method schematic. **a.** Standard normal error ellipse is blue. Arrow indicates a ray from it at angle $\hat{\mathbf{n}}$ in an angular slice $d\hat{\mathbf{n}}$, crossing the gray standardized integration domain $\tilde{f}(z) > 0$ at z_1 and z_2 . **b.** 1d slice of this picture along the ray. The standard normal density along a ray is blue. $\tilde{f}_{\hat{\mathbf{n}}}(z)$ is the slice of $\tilde{f}(z)$, crossing at z_1 and z_2 .

is a quadratic such as eq. 2, its slice by the ray is given by:

$$\begin{aligned}\tilde{q}_{\hat{\mathbf{n}}}(z) &= \tilde{q}(z\hat{\mathbf{n}}) = \hat{\mathbf{n}}' \tilde{\mathbf{Q}}_2 \hat{\mathbf{n}} z^2 + \tilde{\mathbf{q}}_1' \hat{\mathbf{n}} z + \tilde{q}_0 \\ &= \tilde{q}_2(\hat{\mathbf{n}}) z^2 + \tilde{q}_1(\hat{\mathbf{n}}) z + \tilde{q}_0 > 0.\end{aligned}$$

This is a scalar quadratic domain in z that varies with the direction. Fig. 1b is an example of such a domain, where the integration domain is below z_1 (which is negative), and above z_2 .

Note that a sufficient description of the axial domain is to specify whether the ray begins inside the domain, and all the points at which it crosses the domain (so for a quadratic, its overall scale magnitude does not matter). We denote the first by the initial sign $\sigma(\hat{\mathbf{n}}) = \text{sign}(\tilde{f}_{\hat{\mathbf{n}}}(-\infty)) = 1/-1/0$ if the ray begins inside/outside/grazing the integration domain. For a quadratic domain, for example:

$$\sigma(\hat{\mathbf{n}}) = \text{sign}(\tilde{q}_{\hat{\mathbf{n}}}(-\infty)) = \begin{cases} \text{sign}(\tilde{q}_2(\hat{\mathbf{n}})), & \text{if } \tilde{q}_2(\hat{\mathbf{n}}) \neq 0, \\ -\text{sign}(\tilde{q}_1(\hat{\mathbf{n}})), & \text{if } \tilde{q}_2(\hat{\mathbf{n}}) = 0, \\ \text{sign}(\tilde{q}_0), & \text{if } \tilde{q}_2(\hat{\mathbf{n}}) = \tilde{q}_1(\hat{\mathbf{n}}) = 0. \end{cases}$$

The crossing points are the zeros $z_i(\hat{\mathbf{n}})$ of $\tilde{f}_{\hat{\mathbf{n}}}(z) =$

$f(\Sigma^{\frac{1}{2}} \hat{\mathbf{n}} z + \boldsymbol{\mu})$ ($z_i \hat{\mathbf{n}}$ are then the boundary points in the full space). For a quadratic domain $\tilde{q}_{\hat{\mathbf{n}}}(z)$ these are simply its roots. For a general domain, the zeros are harder to compute. Chebyshev polynomial approximations [7] aim to find all zeros of a general function, but can be slow. Other numerical algorithms can find all function zeros in an interval to arbitrary accuracy. We use such an algorithm to find the zeros of $\tilde{f}_{\hat{\mathbf{n}}}(z)$ within $(-m, m)$. This amounts to ray-scanning $f(\mathbf{x})$ within a Mahalanobis distance m of the normal. The error in the integral due to this approximation is therefore $< 2\bar{\Phi}(m)$.

In fig. 1, the initial sign along the ray is 1, and z_1 and z_2 are the crossing points.

Most generally, this method can integrate in any domain for which we can return its ‘scan’ (i.e. the initial sign and crossing points) along any ray $\hat{\mathbf{n}}$. So if a domain is already supplied in this ‘ray-scan’ function form $f_{\text{ray}} : \hat{\mathbf{n}} \rightarrow (\sigma, z_i)$, our method can readily integrate over it. When supplied with quadratic domain coefficients, or a general domain $f(\mathbf{x}) > 0$, the toolbox ray-scans it automatically under the hood.

2.2.3 Standard normal distribution on a ray

In order to integrate over piecewise intervals of z such as fig. 1b, we shall first calculate the semi-definite integral from some z to ∞ , then stitch them together over the intervals.

Consider the probability in the angular slice $d\hat{\mathbf{n}}$ above some positive z such as z_2 in fig. 1a. Note that the probability of a standard normal beyond some radius is given by the chi-square distribution. If Ω_d is the total angle in d dimensions (2 in 1d, 2π in 2d, 4π in 3d), and $F_{\chi_d^2}(x)$ is the chi-square cdf with d degrees of freedom, we have:

$$\Omega_d \int_{z>0}^{\infty} (2\pi)^{-\frac{d}{2}} e^{-\frac{z^2}{2}} dz = 1 - F_{\chi_d^2}(z^2).$$

So the probability in the angular slice $d\hat{\mathbf{n}}$ above a positive z is $\left[1 - F_{\chi_d^2}(z^2)\right] \frac{d\hat{\mathbf{n}}}{\Omega_d}$. Now, for the probability in the angular slice upwards of a negative z (such as z_1), we need to add two probabilities: that in the finite cone from the origin to the point, which is $F_{\chi_d^2}(z^2; d) \frac{d\hat{\mathbf{n}}}{\Omega_d}$, and that in the entire semi-infinite cone on the positive side, which is $\frac{d\hat{\mathbf{n}}}{\Omega_d}$. These sum to $\left[1 + F_{\chi_d^2}(z^2)\right] \frac{d\hat{\mathbf{n}}}{\Omega_d}$. Thus, the probability in an angular slice $d\hat{\mathbf{n}}$ above a positive or negative z is:

$$\underbrace{\left[1 - \text{sign}(z) F_{\chi_d^2}(z^2)\right]}_{=: 2\bar{\Phi}_d^{\text{ray}}(z)} \frac{d\hat{\mathbf{n}}}{\Omega_d}.$$

We denote the distribution of the standard normal along a ray as $\Phi_d^{\text{ray}}(z)$, and its density is $\phi_d^{\text{ray}}(z) = |z| f_{\chi_d^2}(z^2)$. $\phi_1^{\text{ray}}(z) = \phi(z)$, but in higher dimensions it is double-peaked about the origin (fig. 1b), due to the opposing effects of the density falling, but the volume of the angular slice growing, with increasing radius.

2.2.4 Probability in an angular slice

We can now write the total probability in the angular slice of fig. 1 as the sum of terms accounting for the initial sign

and each root. Without roots, this probability would be $d\hat{\mathbf{n}}$ times $\frac{2}{\Omega_d}/\frac{1}{\Omega_d}/0$ accordingly as $\sigma = 1/0/-1$, summarized as $\frac{\sigma(\hat{\mathbf{n}})+1}{\Omega_d}$. To this we add the integral from each root to ∞ , signed according to whether we are entering or exiting the domain at that root:

$$dp(\hat{\mathbf{n}}) = \left[\frac{2}{\Omega_d} - \frac{2\bar{\Phi}_d^{\text{ray}}(z_1)}{\Omega_d} + \frac{2\bar{\Phi}_d^{\text{ray}}(z_2)}{\Omega_d} \right] d\hat{\mathbf{n}}.$$

The sign of the first root term is always opposite to σ , and subsequent signs alternate as we enter and leave the domain. In general then:

$$dp(\hat{\mathbf{n}}) = \underbrace{\left[\sigma(\hat{\mathbf{n}}) + 1 + 2\sigma(\hat{\mathbf{n}}) \sum_i (-1)^i \bar{\Phi}_d^{\text{ray}}(z_i(\hat{\mathbf{n}})) \right]}_{\alpha(\hat{\mathbf{n}})} \frac{d\hat{\mathbf{n}}}{\Omega_d}$$

Thus, the axial integral is $\frac{\alpha(\hat{\mathbf{n}})}{\Omega_d}$. The total probability $\frac{1}{\Omega_d} \int \alpha(\hat{\mathbf{n}}) d\hat{\mathbf{n}}$ can be computed, for up to 3d, by numerically integrating $\alpha(\hat{\mathbf{n}})$ over a grid of angles spanning half the angular space (since we account for both directions of a ray), using any standard scheme. An adaptive grid can match the shape of the integration boundary (finer grid at angles where the boundary is sharply changing), and also set its fineness to evaluate the integral to a desired absolute or relative precision. Fig. 2a illustrates integrating a trivariate normal with arbitrary covariance in an implicitly-defined toroidal domain $f_i(\mathbf{x}) = a - \left(b - \sqrt{x_1^2 + x_2^2} \right)^2 - x_3^2 > 0$.

Beyond 3d, we can use Monte Carlo integration over the angles. We draw a sample of \mathbf{z} 's from the standard normal in those dimensions, then $\hat{\mathbf{n}} = \frac{\mathbf{z}}{\|\mathbf{z}\|}$ is a uniform random sample of rays, over which the expectation $\langle \alpha(\hat{\mathbf{n}}) \rangle_{\hat{\mathbf{n}}}/2$ is the probability estimate. Fig. 2a shows the computation of the 4d standard normal probability in the domain $f_p(\mathbf{x}) = \sum_{i=1}^4 |x_i| < 1$, a 4d extension of a regular octahedron with plane faces meeting at sharp edges.

Since the algorithm already computes the boundary points over its angular integration grid, they may be stored for plotting and inspecting the boundary. Rather than an adaptive integration grid though, boundaries are often best visualized over a uniform grid (uniform array of angles in 2D, or a Fibonacci sphere in 3D [8]), which we can explicitly supply for this purpose.

2.2.5 Probabilities of any function of a normal vector

We previously mentioned the equivalent ‘normal probability’ and ‘function probability’ pictures of conceptualizing a normal integral. So far we have mostly used the normal probability notion, seeing scalar functions $f(\mathbf{x})$ as defining integral domains of the normal \mathbf{x} . But in the function probability picture, $f(\mathbf{x})$ is instead seen as a mapping from the multiple variables \mathbf{x} to a single one, which can be considered a decision variable. Hence, integrating the normal in the multi-dimensional domain $f(\mathbf{x}) > 0$ corresponds to integrating the 1d pdf of the decision variable $f(\mathbf{x})$ beyond 0. It is helpful to plot this 1d pdf, especially when there are too many

dimensions of \mathbf{x} to visualize the normal probability picture. Conversely, given any scalar function $f(\mathbf{x})$ of a normal, its cdf, $F_f(c) = p(f(\mathbf{x}) < c)$, is computed as the normal probability in the domain $c - f(\mathbf{x}) > 0$. Differentiating this gives us the pdf. Insets of figs. 2a and b show the 1d pdf's, computed in this way, of the toroidal function in 3d and the polyhedral function in 4d. Also, inverting the function cdf using a numerical root-finding method gives us its inverse cdf (percentage points). Using these we can compute, for example, that if x and y are jointly normal with $\mu_x = 1$, $\mu_y = 2$, $\sigma_x = .1$, $\sigma_y = .2$, and $\rho_{xy} = .8$, then the mean, median and sd of x^y are respectively 1.03, 1 and 0.21.

Now consider the joint distribution of a vector (multi-valued) function of the normal, e.g. $\mathbf{f}(\mathbf{x}) = [f_1(\mathbf{x}), f_2(\mathbf{x})]$. The probability of this function in some \mathbf{f} -domain is again the normal probability in a corresponding \mathbf{x} -domain. For example, the joint cdf $F_{\mathbf{f}}(c_1, c_2)$ is the function probability in an explicit domain: $p(f_1 < c_1, f_2 < c_2)$, and can be computed as the normal probability in the intersection of the \mathbf{x} -domains $f_1(\mathbf{x}) < c_1$ and $f_2(\mathbf{x}) < c_2$, i.e. the domain $\min(c_1 - f_1(\mathbf{x}), c_2 - f_2(\mathbf{x})) > 0$. Numerically computing $\frac{\partial}{\partial c_1} \frac{\partial}{\partial c_2} F_{\mathbf{f}}(c_1, c_2)$ then gives the joint pdf of the vector function. Fig. 2c, left, is an example of a joint pdf of two functions of a bivariate normal, computed in this way. The probability of such a vector function in an implicit domain, i.e. $p(g(\mathbf{f}) > 0)$, is computed as the normal probability in the implicit domain: $p(h(\mathbf{x}) > 0)$ where $h = g \circ \mathbf{f}$. As an example, fig. 2c illustrates the function probability and normal probability pictures of the implicit integral $p(x_1 \sin x_2 - x_2 \cos x_1 > 1)$. The 83rd percentile of this function (using the inverse cdf) is 4.87.

3 Classifying normal samples

Suppose observations come from several normal distributions with parameters $\boldsymbol{\mu}_i, \boldsymbol{\Sigma}_i$ and priors p_i , and the outcome values (rewards and penalties) of classifying them are represented in a matrix \mathbf{V} : v_{ij} is the value of classifying a sample from i as j .

If the true class is i , selecting i over others provides a relative value gain of $v_i := v_{ii} - \sum_{j \neq i} v_{ij}$. Given a sample \mathbf{x} , the expected value gain of deciding i is therefore $\langle v(i|\mathbf{x}) \rangle = p(i|\mathbf{x})v_i = p(\mathbf{x}|i)p_i v_i$. The Bayes-optimal decision is to assign each sample to the class that maximizes this expected value gain, or its log:

$$\ln \langle v(i|\mathbf{x}) \rangle = -\frac{1}{2}(\mathbf{x} - \boldsymbol{\mu}_i)' \boldsymbol{\Sigma}_i^{-1} (\mathbf{x} - \boldsymbol{\mu}_i) + \ln \frac{p_i v_i}{\sqrt{|\boldsymbol{\Sigma}_i|} (2\pi)^d}.$$

When the outcome value is simply the correctness of classification, $\mathbf{V} = \mathbf{1}$ (so each $v_i = 1$), then this quantity is the log posterior, $\ln p(i|\mathbf{x})$.

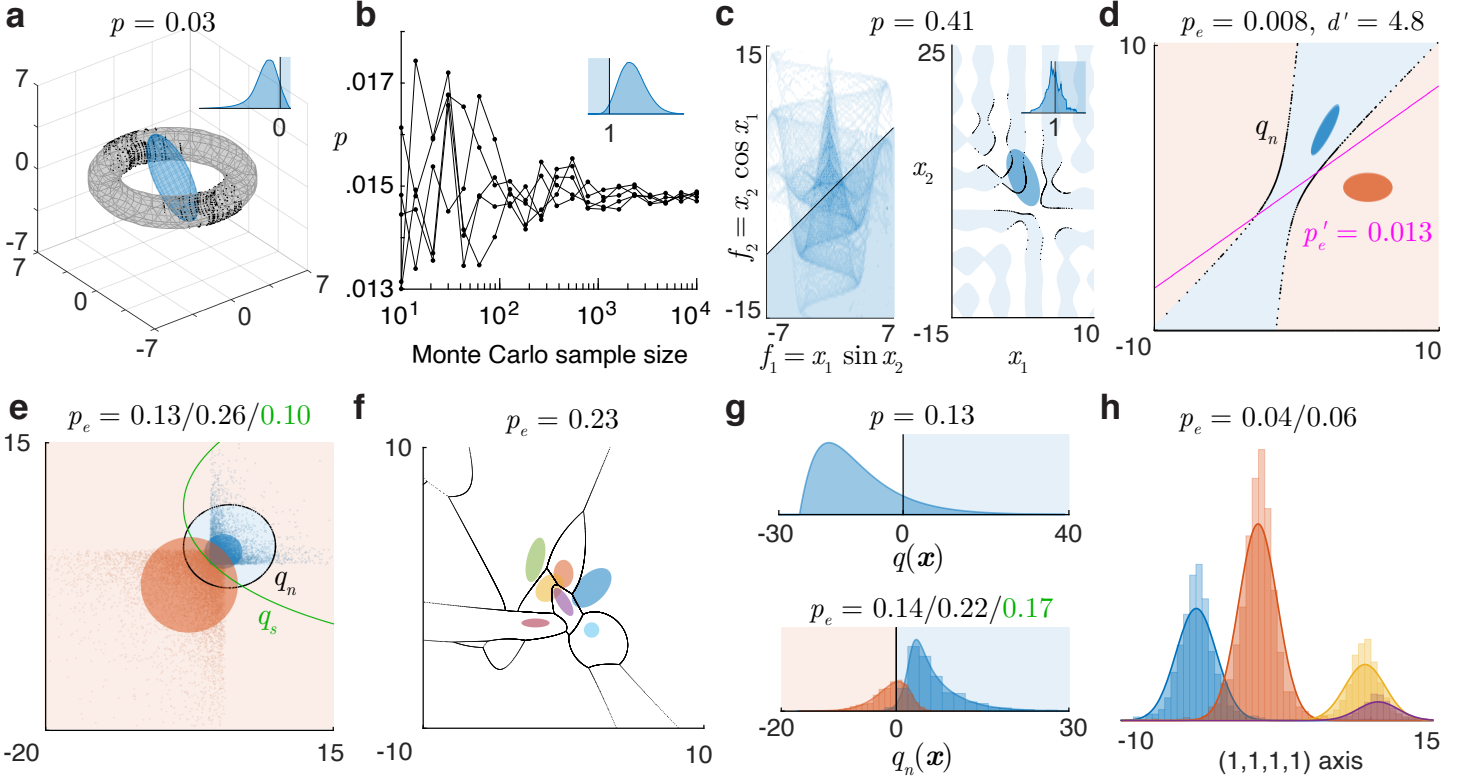


Figure 2: Toolbox outputs for some integration and classification problems. **a.** The probability of a 3d normal (blue shows 1 sd error ellipsoid) in an implicit toroidal domain $f_t(\mathbf{x}) > 0$. Black dots are boundary points within 3 sd scanned by the ray method, across Matlab’s adaptive integration grid over angles. Inset: pdf of $f_t(\mathbf{x})$ and its integrated part (blue overlay). **b.** Monte Carlo estimates of the 4d standard normal probability in a 4d polyhedral domain $f_p(\mathbf{x}) < 1$, across multiple runs, converging with growing sample size. Inset: pdf of $f_p(\mathbf{x})$ and its integrated part. **c.** Left: heat map of joint pdf of two functions of a 2d normal, to be integrated over the implicit domain $f_1 - f_2 > 1$ (overlay). Right: corresponding integral of the normal (blue error ellipse) over the domain $h(\mathbf{x}) = x_1 \sin x_2 - x_2 \cos x_1 > 1$ (blue regions), ‘scanned’ up to 3 sd (black dots). Inset: pdf of $h(\mathbf{x})$ and its integrated part. **d.** Classifying two 2d normals using the optimal boundary q_n (which provides the d'), and a custom linear boundary. **e.** Classification based on samples (dots) from non-normal distributions. Filled ellipses are error ellipses of fitted normals. q_s is an optimized boundary between the samples. The three error rates are: of the normals with q_n , of the samples with q_n , and of the samples with q_s . **f.** Classifying several 2d normals with arbitrary means and covariances. **g.** Top: 1d projection of a 4d normal integral over a quadratic domain $q(\mathbf{x}) > 0$. Bottom: 1d projection of classifying two 4d normals based on samples, with unequal priors, and unequal outcome values (correctly classifying the blue class is valued 4 times the red, hence the optimal criterion is shifted). Histograms and smooth curves are the projections of the samples and the fitted normals. The sample-optimized boundary q_s cannot be plotted on this q_n axis. **h.** Classification based on four 4d non-normal samples, with different priors and outcome values, projected on the axis along $(1,1,1,1)$. The boundaries cannot be projected to this axis.

3.1 Two classes

If there are only two normal classes a and b , the optimal decision is to pick a if

$$\ln \frac{\langle v(a|\mathbf{x}) \rangle}{\langle v(b|\mathbf{x}) \rangle} = q_n(\mathbf{x}) = \mathbf{x}'\mathbf{Q}_2\mathbf{x} + \mathbf{q}'_1\mathbf{x} + q_0 > 0, \text{ where:}$$

$$\begin{aligned} \mathbf{Q}_2 &= \frac{1}{2} (\boldsymbol{\Sigma}_b^{-1} - \boldsymbol{\Sigma}_a^{-1}), \\ \mathbf{q}_1 &= \boldsymbol{\Sigma}_a^{-1}\boldsymbol{\mu}_a - \boldsymbol{\Sigma}_b^{-1}\boldsymbol{\mu}_b, \\ q_0 &= \frac{1}{2} \left(\boldsymbol{\mu}'_b\boldsymbol{\Sigma}_b^{-1}\boldsymbol{\mu}_b - \boldsymbol{\mu}'_a\boldsymbol{\Sigma}_a^{-1}\boldsymbol{\mu}_a + \ln \frac{|\boldsymbol{\Sigma}_b|}{|\boldsymbol{\Sigma}_a|} \right) + \ln \frac{p_a v_a}{p_b v_b}. \end{aligned} \quad (3)$$

This quadratic $q_n(\mathbf{x})$ is the Bayes decision variable to classify two normals (when $\mathbf{V} = \mathbf{1}$, it is the log posterior ratio). The classification outcome probabilities (error rates) of different types, i.e. true and false positives and negatives, are the probabilities of the normals on either side of this quadratic boundary, which can be computed using the methods we discussed. The overall error rate p_e is the prior-weighted sum of the error rates of each normal.

When both normals have the same covariance matrix, the same linear transform changes both to unit spheres, so their discriminability d' is simply the Mahalanobis distance between them. With different covariances, no linear transform can change both to unit spheres, so d' is ill-defined, thus limiting its use to equal-covariance cases. But we can gen-

erally define $d' = -2\Phi^{-1}(p_e)$ (with p_e computed with equal priors, $\mathbf{V} = \mathbf{1}$, and the optimal boundary), which is the separation between two unit variance normals with the same overlap. This definition of d' extends to all cases (including equal means) as a smooth function of the layout and shapes of the normals, and reduces to the Mahalanobis distance for equal covariance.

3.2 Custom classifiers

Sometimes, instead of the optimal classifier, we need to test and compare sub-optimal classifiers, e.g. one that ignores a cue, or some cue covariances, or a simple linear classifier. For this reason, the toolbox allows the user to extract the optimal boundary, change it, and explicitly supply some custom boundary to use in place of the optimal boundary. Fig. 2d compares the classification of two bivariate normals using the optimal boundary (which provides the d'), vs. using a hand-supplied linear boundary. Just as with integration, one can supply custom classification domains in ray-scan or implicit form.

3.3 Classifying using data

If instead of normal parameters, we have labelled data as input, we can estimate the parameters. The maximum-likelihood estimates of the means, covariances and priors of normals are simply the sample means, covariances and relative frequencies. With these estimated parameters we can compute the optimal classifier $q_n(\mathbf{x})$ and the error matrix. We can further calculate another quadratic boundary $q_s(\mathbf{x})$ to separate the given samples even better: we start with $q_n(\mathbf{x})$, then optimize its $(d+1)(d+2)/2$ independent parameters to maximize the classification outcome value of the given samples. This is especially helpful with non-normal data, where the optimal boundary between estimated normals is not the best classifier. This optimization then improves classification while still staying within the smooth quadratic family and preventing overfitting. Fig. 2e shows classification based on labelled non-normal samples.

If, along with labelled samples, we supply a custom quadratic classifier, the toolbox instead optimizes this for the sample. This is useful, say, in the following case: suppose we have already computed the optimal classifier for samples in some feature space. Now if we augment the data with additional features, we may start from the existing classifier (with its coefficients augmented with zeros in the new dimensions) to find the optimal classifier in the larger feature space.

3.4 Multiple classes

The optimal decision boundary between two normals is a quadratic, hence classification error rates can be computed using the generalized chi-square method or the ray method. When classifying amongst more than two normals, the decision region for each normal is the intersection of its quadratic decision regions $q_n^i(\mathbf{x}) > 0$ with all the other normals i , and

may be written as:

$$f(\mathbf{x}) = \min_i q_n^i(\mathbf{x}) > 0.$$

This is not a quadratic, so only the ray method can compute the error rates here. For a ray through this domain, the initial sign is $\sigma = \min_i \sigma_i$, and the roots are found by collecting those roots of each quadratic where every other quadratic is positive. Fig. 2f shows the classification of several normals with arbitrary means and covariances.

3.5 Reducing dimensions

Reducing a many-dimensional integration or classification problem to fewer dimensions allows visualization. Projecting a normal \mathbf{x} to an axis, or mapping \mathbf{x} to its Mahalanobis distance (related to its log probability), are ways to project the distribution to 1d. However, in an integration problem of finding $p(f(\mathbf{x}) > 0)$, these will not uniquely map the integration domain boundary $f(\mathbf{x}) = 0$. Instead, in light of our previous discussion, we can map $\mathbf{x} \rightarrow f(\mathbf{x})$, which maps the problem to the 1d function probability picture of integrating the pdf of $f(\mathbf{x})$ above 0. For quadratic integrations beyond 3d, the toolbox plots the pdf of this projection $q(\mathbf{x})$ (fig. 2g, top), which is a quadratic function of a normal, so distributed as a generalized chi-square.

Similarly, for a 2-normal classification using a classifier $f(\mathbf{x}) = 0$, mapping $\mathbf{x} \rightarrow f(\mathbf{x})$ projects it to a 1d classification on the decision variable axis with the boundary at 0, with all classification errors preserved. For the default optimal classification, the toolbox shows the projection to the Bayes decision variable $\mathbf{x} \rightarrow q_n(\mathbf{x})$, which is distributed as a generalized chi-square (fig. 2g, bottom). For a many-dimensional problem, we can define a decision variable on a subset of dimensions and merge them into one, then merge those further etc, as we shall demonstrate later. With multiple classes, there is no single decision variable to project to, but the toolbox plots the projection along any chosen axis. Fig. 2h shows the classification using normal fits to samples from four 4d t distributions, projected onto the axis along $(1,1,1,1)$.

3.6 Testing normal approximations

The results developed here are for normal distributions. But even when the variables in a classification problem are not exactly normal (i.e. have an empirical or some other known theoretical distribution), we can still use these results if we check that normals are an adequate approximation, i.e. an equivalence test. One test is to project the distributions to one dimension, either by mapping to a quadratic form (fig. 2g), or to an axis (fig. 2h), where we can visually compare the observed distributions and their fitted normals.

We could further explicitly test the normality of the variables with measures like negentropy, but often this is stricter than needed. For example, if the final test of the normal approximation is against outcomes of a limited-trials classification experiment, it suffices to check that it predicts similar enough performance as the true distributions with the given

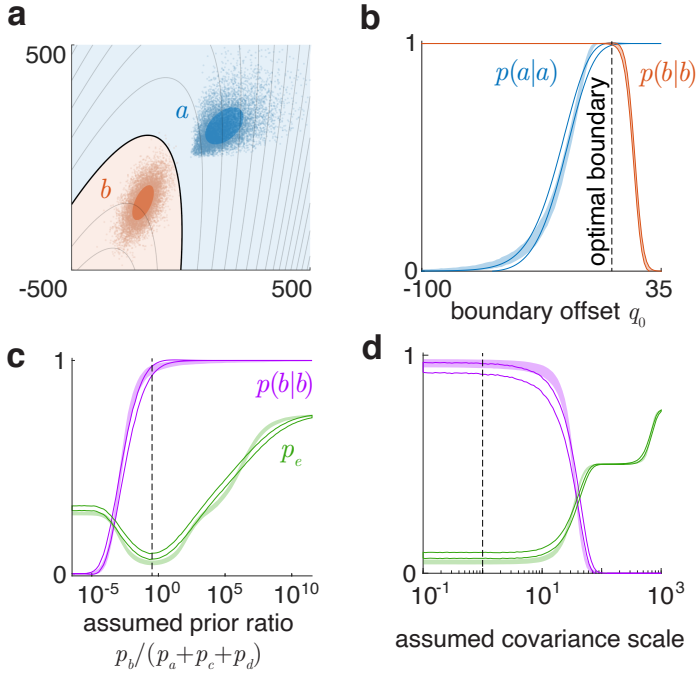


Figure 3: Testing normal approximations for classification. **a.** Classifying two empirical distributions (a is not normal). Gray curves are a family of suboptimal boundaries. **b.** Mean \pm sd of hits and correct rejections observed (color fills) vs. predicted by the normal model (outlines), along this family of boundaries. **c.** Similar bands for class b hits and overall error, for the 4d 4-class problem of fig. 2h, across boundaries assuming different priors p_b , and **d.** across boundaries assuming different covariance scales (d' s).

number of trials. For any classification boundary, we can calculate outcome rates, e.g. $p(a|a)$ for a hit, determined from the true distributions, vs. from the normal approximations. The count of hits in a task is binomial with parameters equal to the number of a trials and $p(a|a)$, so we can compare its count distribution between the true and the normal model.

If the classes are well-separated (e.g. for ideal observers), the optimal boundary often provides near-perfect accuracy on both the true and the normal distributions, so the comparison yields no insight. We thus extend this test across two kinds of common suboptimal boundaries that cut through regions of error and show decisively if the normal approximation still holds up. The first kind corresponds to a model or subject being biased towards one type of error or another, i.e. a change in the assumed ratio of priors or outcome values, reflecting in a shifted offset q_0 of the boundary (eq. 3). The second kind is the observer having an internal d' different from the true (external) one (e.g. due to blurring by internal noise), so adopting a boundary corresponding to covariance matrices that are scaled (by s , say), which again shifts q_0 , by $\frac{s-1}{2} \ln \left| \frac{\Sigma_b}{\Sigma_a} \right|$. Thus, with two classes, both kinds of suboptimal boundaries are described by varying q_0 .

Fig. 3a shows the classification of two empirical distributions, where a is not normal, and gray curves show this family of boundaries. Fig. 3b shows the mean \pm sd of

error rates from applying these boundaries on samples of 100 trials (typical of a psychophysics experiment) from each true distribution, vs. the normal approximations. They exactly coincide for $p(b|b)$, but deviate for $p(a|a)$, correctly reflecting that b is normal but a is not. The investigator can judge if this deviation is still small enough for their purpose. Plots like these convey similar information to an ROC curve [1] when the two distributions overlap substantially.

Fig. 3c shows similar tests for the 4d 4-class problem of fig. 2h, with priors now equal. The family of boundaries corresponds to varying the assumed prior p_b . We may look at any of the 16 error rates here, e.g. $p(b|b)$, and also the overall error p_e . With multiple classes, the numbers of different outcomes for trials of a class are multinomially distributed, so that the number of its wrong outcomes is again binomially distributed. p_e is the prior-weighted sum of these, so we can calculate its mean and sd predicted by the observed vs. the normal distributions. Fig. 3d shows the test across boundaries corresponding to all covariance matrices scaled by a factor, changing the d' between the classes.

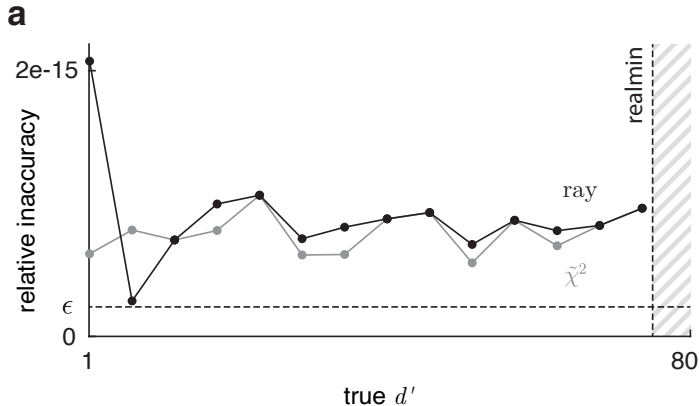
Some other notable suboptimal boundaries to consider for this test are ones that correspond to additive independent noise to the cues (which changes only their variances but not their covariances), ones that ignore certain cues or cue covariances, or simple flat boundaries. As seen here, even for many-dimensional distributions that cannot be visualized, these tests can be performed to reveal some of their structure, and to show which specific outcomes deviate from normal prediction for which boundaries.

When the problem variables have a known non-normal theoretical distribution, the best normal approximation is the one that matches its mean and covariance, and these tests can be performed by theoretically calculating or bootstrap sampling the error rate distributions induced by the known true variable distributions.

4 Toolbox functions

For an integration problem, the toolbox provides a function that inputs the normal parameters and the integration domain (as quadratic coefficients or a ray-scan or implicit function), and outputs the integral and its complement, the boundary points computed, and a plot. The function for a classification problem inputs normal parameters, priors, outcome values and an optional classification boundary, and outputs the boundary q_n and points on it, the error matrix and d' of the normals with q_n , and a plot. With sample input, it additionally returns q_s and points on it, error matrices and d' s of the samples with q_n and q_s , and the mapped decision variables $q_n(\mathbf{x})$ and $q_s(\mathbf{x})$ from the samples. The toolbox also provides functions to compute pdf's, cdf's and inverse cdf's of functions of normals.

Each problem discussed in this paper (examples of fig. 2, tests of figs. 3 and 4, and research applications in fig. 5) is available as a demo in the 'getting started' live script of the toolbox, and can be easily adapted to other problems.



a

Problem	Rel. diff.	$t_{\tilde{\chi}^2}$ (s)	t_{ray} (s)
2d, p_e	0	.60	.16
2d, p'_e	2.6e-16	.0098	.12
2e, 1 st p_e	3.6e-6	1.5	.20
2g, p	0	.44	1.3
2g, 1 st p_e	0	.63	.49

b

Figure 4: Performance benchmarks of the two algorithms. **a.** Relative inaccuracies in d' estimates by the two methods against known ground truth, with increasing separation. ϵ is machine epsilon. The largest computable $d' \approx 75$, corresponding to the smallest representable error ('realmin'). **b.** For the quadratic-boundary problems of fig. 2, relative differences in the outputs of the two methods, and their computation times for 1% precision.

5 Performance benchmarks

A variety of techniques are built into the algorithms to preserve accuracy, such as holding tiny and large summands separate to prevent rounding, using symbolic instead of numerical calculations, and using accurate tail probabilities. We first test for accuracy against known ground truth at the limit of high d' where it is most challenging (which occurs for computational models and ideal observers with high discriminability). We take two 3d normals with the same covariance matrix, so that the true d' is simply their Mahalanobis distance. We increase their separation, while computing the optimal error with both methods at maximum precision, then a \hat{d}' from it. Fig. 4a shows the relative inaccuracies $|\hat{d}' - d'|/d'$ as true d' increases. Inaccuracies in both methods are equally negligible, do not grow with increasing separation, and are in fact of the order of the double-precision machine epsilon ϵ , demonstrating that neither algorithm contains any error source besides machine imprecision. $d' \approx 75$ corresponds to the smallest error rate p_e representable in double-precision ('realmin' = 2e-308), beyond which both methods return $p_e = 0$ and $\hat{d}' = \infty$.

Second, for problems with no ground truth but quadratic boundaries, we can check the two methods for agreement. For such problems in fig. 2, we compute the values (integrals or error rates) $v_{\tilde{\chi}^2}$ and v_{ray} up to practicable precisions $\Delta v_{\tilde{\chi}^2}$

and Δv_{ray} . If they are equal within error, i.e. $|v_{\tilde{\chi}^2} - v_{\text{ray}}| < \Delta v_{\tilde{\chi}^2} + \Delta v_{\text{ray}}$, we call their relative difference as 0, otherwise it is $|v_{\tilde{\chi}^2} - v_{\text{ray}}| / ((v_{\tilde{\chi}^2} + v_{\text{ray}}) / 2)$. Table 4b lists these, along with the times to compute each to 1% precision. The methods produce nearly identical values at comparable speeds.

6 Applications in visual object detection

We demonstrate the use of these methods in visual detection tasks with multiple correlated cues with different variances.

6.1 Detecting targets in natural scenes

We have applied this method in a study to measure how humans compare against a nearly ideal observer in detecting occluding targets against natural scene backgrounds in a variety of conditions [9]. We placed a target on a random subset of natural images, then blurred and downsampled them to mimic the effect of the early visual system (fig. 5a). We sought to measure how well the targets on these degraded images can be detected using three cues: related to the luminance in the target region, the target pattern, and the target boundary. We computed these cues on the set of images. They form two approximately trivariate normal distributions for the target present vs. absent categories. We then computed the decision boundary, error rate and d' against varying conditions. Fig. 5b shows the result for one condition, with a hyperboloidal boundary. These error rates and d' s can then be compared across conditions.

6.2 Detecting camouflage

We also applied this method in a study measuring performance in detecting camouflaged objects [10]. The major source of information for detecting the object (e.g., fig. 5c) is its edge, which we compute at scales of 2px, 4px and 8px. We extract two scalar features from the edge at each scale: the edge power captures its overall prominence, and the edge spectrum characterizes how this prominence is distributed along the boundary. We thus have 6 total features. Fig. 5d shows the classification of these images using these 6 features. We see from this projection that the a distribution is quite normal, whereas b is nearly so. Consistently, in a normality test for classification with 100 trials, fig. 5e, $p(b|b)$ deviates marginally from its normal prediction, but cannot be told apart much with this number of trials, so we accept the normal approximation here. Fig. 5f shows the classification using only the cues at the 2px scale. We use our dimension reduction technique to merge these two cues into one: $\mathbf{x} \rightarrow q_s(\mathbf{x})$, which we call simply the edge cue. Classifying with a 0 criterion on this, fig. 5g, is the same as the 2d classification of fig. 5f, and preserves the errors. We do the same merging at 4px and 8px, thus mapping 6 features to 3. Fig. 5h shows the classification using these 3 merged features. Due to the information in the two added scales,

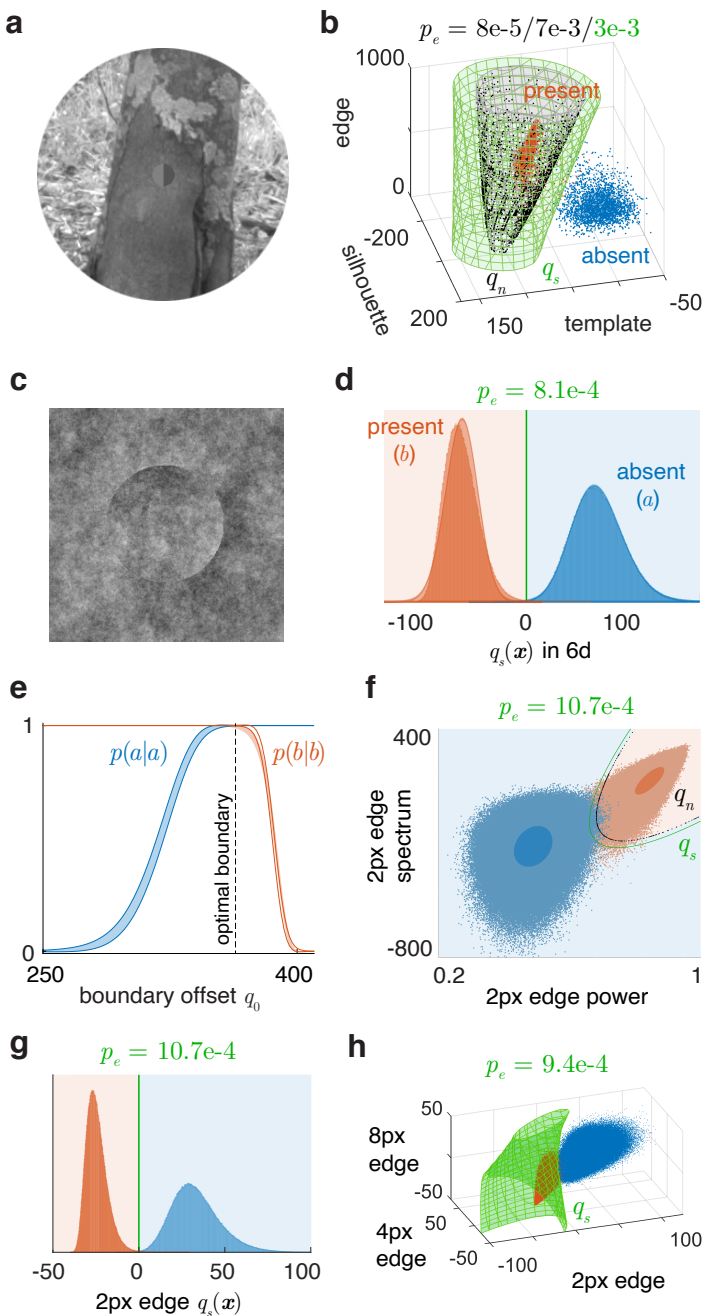


Figure 5: Applying the method and toolbox to visual target detection studies. **a.** Example image of a target on a natural background. **b.** Classification of images with the target present or absent, in the space of three cues. Black dots are the boundary points computed for integration. **c.** Example image for camouflage detection. **d.** Classifying these using 6 cues, mapped to 1 using the sample-optimized quadratic. **e.** Bootstrap mean \pm sd of hit and correct rejection fractions from applying a family of offset boundaries on 100 samples of the true 6d cue distributions (color fills), vs. their normal approximations (outlines). **f.** Classifying with only two cues computed at 2px. **g.** Merging the two cues of plot f into one using the sample-optimized quadratic. **h.** Classifying with such merged cues at 3 scales.

the classification has improved. The total number of classifier parameters used in this sequential classification is 28 (6 for each of the three 2d classifiers, then 10 when combining them in 3d). The classifier in full 6d has 28 parameters as well, yet is better since it can simultaneously optimize them all. Even so, merging features allows one to combine them in groups and sequences according to the problem logic, and also visualize their lower-dimensional spaces.

7 Acknowledgements

We are thankful to Dr. R Calen Walshe (University of Texas at Austin) for helpful discussions, and Dr. Johannes Burge (University of Pennsylvania) for discussions, checks and improvements in the method and code. This work was supported by NIH grants EY11747 and EY024662.

References

- [1] David Marvin Green, John A Swets, et al. *Signal detection theory and psychophysics*, volume 1. Wiley New York, 1966.
- [2] Richard O Duda, Peter E Hart, and David G Stork. *Pattern classification*. John Wiley & Sons, 2012.
- [3] Harold Ruben. Probability content of regions under spherical normal distributions, i. *The Annals of Mathematical Statistics*, 31(3):598–618, 1960.
- [4] Alan Genz and Frank Bretz. *Computation of multivariate normal and t probabilities*, volume 195. Springer Science & Business Media, 2009.
- [5] Harold Ruben. Probability content of regions under spherical normal distributions, iv: The distribution of homogeneous and non-homogeneous quadratic functions of normal variables. *The Annals of Mathematical Statistics*, 33(2):542–570, 1962.
- [6] Robert B Davies. Numerical inversion of a characteristic function. *Biometrika*, 60(2):415–417, 1973.
- [7] Lloyd N Trefethen. *Approximation theory and approximation practice*, volume 164. Siam, 2019.
- [8] Edward B Saff and A BJ Kuijlaars. Distributing many points on a sphere. *The mathematical intelligencer*, 19(1):5–11, 1997.
- [9] R Calen Walshe and Wilson S Geisler. Detection of occluding targets in natural backgrounds. *Journal of Vision*, 20(13):14, 2020.
- [10] Abhranil Das and Wilson Geisler. Understanding camouflage detection. *Journal of Vision*, 18(10):549, 2018.